Journal of Applied Fluid Mechanics, Vol. 16, No. 8, pp. 1560-1573, 2023.
Available online at www.jafmonline.net, ISSN 1735-3572, EISSN 1735-3645.
https://doi.org/10.47176/jafm.16.08.1676

Numerical Investigation of Bed Shear Stress and Roughness Coefficient Distribution in a Sharp Open Channel Bend

P. Hu and M. Yu†

State Key Laboratory of Water Resources and Hydropower Engineering, Wuhan University, Wuhan 430072, China

†*Corresponding author. Email address: mhyu@whu.edu.cn*

ABSTRACT

The helical flow leads to the redistribution of the bed shear stress and roughness coefficient in open-channel bends, influencing the transport of sediment and riverbed evolution process. To explore the mechanisms underlying this redistribution, a 3D numerical simulation of a 180° sharp bend was performed by solving the Reynolds-averaged Navier–Stokes (RANS) equations using the Reynolds stress equation model (RSM) as the anisotropic turbulence closure approach. The results indicate that the high bed shear stress zone appeared in the inner bank region from the 50° to 110° sections, and the section maximum bed shear stress gradually shifted outwards, owing to the advective momentum transport by the circulation cells. The quantitative analyses of the terms in depth-averaged Navier-Stokes equations indicate that the contributions of the cross-stream circulation and cross-flow to the downstream bed shear stress were of the same order of magnitude, and the overall contribution rate of the cross-stream circulation was 20%. The contribution rates of the cross-flow, cross-stream circulation, turbulence, and pressure gradient to the transverse bed shear stress were approximately 30%, 7%, 3%, and 60%, respectively, indicating that the pressure gradient term arising from the transverse water surface slope played a dominant role. The Chezy resistance coefficient showed an overall decreasing trend along the bend. Therefore, an effective expression considering the streamwise variation along the centreline and transverse variation was successfully established to predict the uneven distribution of the Chezy resistance coefficient.

Article History

Received November 19, 2022
Revised March 20, 2023
Accepted March 27, 2023
Available online May 31, 2023

Keywords:

Open-channel bends
Reynolds stress equation model
Bed shear stress distribution
Momentum transport
Roughness coefficient

1. INTRODUCTION

Bed shear stress is fundamental in the study of sediment dynamics. It plays a key role in sediment transport processes, including the associated erosion and deposition phenomena in alluvial channels (Krishnappan & Engel, 2004; Vaghefi et al., 2016). The roughness coefficient is widely applied in numerical models for parameterising bed shear stress. In meandering channels, the flow field is highly three-dimensional, owing to the existence of a helical flow, which is initiated by the imbalance of inertial forces and transverse pressure gradients. Recent laboratory and field experiments on the flow structure in river bends indicated that in addition to the primary circulation cell, a reversed circulation cell called the outer-bank cell, often appears in the upper part near the outer bank (Farhadi et al., 2018). The streamwise velocities are redistributed due to the advective momentum transport by circulation cells (Blanckaert & Graf, 2004). Abduo et al. (2021) found that the velocity distribution in the curved open channel is distinguished by the maximum velocity that shifts from a bank to another. Ottevanger et al. (2012) also observed that the maximum velocity always occurs along the inner wall of the bend until it is transported towards the outer wall at the bend exit. Vaghefi et al. (2014) found that high velocities at the beginning of the bend lead to a sharp increase in stress in the beginning sections of the sharp bend. Hence, the effect of these circulation cells and velocity distribution on the flow pattern should be considered to predict bed shear stress in the river bends (Vaghefi et al., 2016). Nanson (2010) also reported that small helices with reversed rotation at the outer banks diverted the regions of maximum shear stress away from the outer bank.

A field study by Dietrich et al. (1979) indicated that the maximum bed shear stress zone was located in the inner bank in the upstream portion, and it also crosses the outside bank upon its penetration into the central segment of the bend. This finding was similar to that of the

NOMENCLATURE

B	channel width	v_n	transverse velocity
c	Chezy resistance coefficient	v_n^*	local deviation from depth-averaged transverse velocity
D_{84}	grain diameter	y_i	simulation value
Fr	Froude number	$\hat{y}_i$	measured value
f, g, h	functions	$\overline{y}_i$	average measured value
h	local water depth	$y_{\max}$	maximum measured value
H	mean water depth	$y_{\min}$	minimum measured value
k	turbulent kinetic energy	δ_{ij}	Kronecker delta
k_s	effective bed roughness	Δy	normal distance to the wall
p	pressure	ε	turbulent dissipation rate
P_{ij}	production of turbulent kinetic energy	θ_τ	angular deviation
Q	discharge	θ	angle between local section and entry section
r	local radius of curvature	θ_0	centre angel of bend
R	radius of curvature of the channel centreline	κ	Von Karman constant
Re	Reynolds number	μ	dynamic viscosity
s, n, z	cylindrical coordinate system	μ_t	eddy viscosity
S	bed slope	υ	kinematic viscosity
u_τ	friction velocity	τ	total bed shear stress
u_i	time-averaged velocity	τ_{bs}	downstream component of bed shear stress
u_i'	fluctuating velocity	τ_{bn}	cross-stream component of bed shear stress
U	mean velocity	ρ	fluid density
v_s	streamwise velocity	Φ_{ij}	pressure strain term

laboratory experiment conducted by Hooke (1975). The bed shear stress distribution is influenced by the channel geometry and flow conditions, and a decrease in the aspect ratio often results in an increase in the magnitude of the bed shear stress. Kashyap et al. (2012) found that the position of regions with high bed shear stress were strongly dependent on the bend curvature. Ippen and Drinker (1962) determined the relationship between the radius of curvature and maximum shear stress, and it was revealed that the flow characteristics of sharp bends differed from the moderate curvature bends (Hu et. al., 2019; Blanckaert, 2011). As bend sharpness represents the ratio of the radius of the curvature of the channel centreline (R) to the channel width (B), mildly curved bends would have a value of O (10) or larger based on the curvature ratio (R/B) as an order of magnitude, whereas, it would be smaller than 3 for sharp bends (Crosato, 2008). Yen and Ho (1990) found that when R/B>3.5, the shear stress distribution at the entrance of the bend was almost always constant, and the maximum bed shear stress appeared in the outer bank region at the exit. Meanwhile, it occurred both in the outer bank region at the exit and in the inner bank region at the beginning of the bend when R/B<3.5. In sharp open-channel bends, higher velocities induce an enhanced water surface superelevation. The corresponding transverse pressure gradient drives larger outer-bank cells to have greater associated bed shear stresses (Nanson, 2010). Moreover, pronounced flow separation occurring in sharp bends also alters the distribution of bed shear stress. Despite its practical importance, the underlying mechanism of the distribution of bed shear stress has remained poorly understood. Here, the effect of circulation cells on hydraulic resistance should be considered, as pronounced transverse variations of the roughness coefficient have important implications in numerical modelling, as indicated by Blanckaert (2015) using depth-averaged flow models. For sharp bends, analysing the wide variation in the roughness coefficient is needed.

The bed shear stress can be determined using experimental measurements obtained via Preston tubes. It is evaluated based on velocity profiles assumed to be in the form of a log-wake law in near-wall regions (Thompson et al., 2003; Kim et al., 2000). Empirical equations that associated it with turbulent kinetic energy or Reynolds shear stress were also proposed by Galperin et al. (1988) and Dey & Das (2012). Vaghefi et al. (2016) found the turbulent kinetic energy methods showed smaller values in bed shear stress calculation compared to the Reynolds method. Blanckaert and De Vriend (2005) investigated the turbulence structure in bend flow and found that it is different from straight uniform flow, in that the Reynolds stress tensor is more diagonally dominant. This is the main cause of the observed reduction of turbulence activity in the outer bend. Constantinescu et al. (2011) observed a large amplification of the turbulent kinetic energy inside the cores of some of these streamwise-oriented vortices. Van Balen et al. (2009) also found that the outer bank cell forms a region of a local increase of turbulent kinetic

energy and of its production and the bed shear stresses are amplified in the bend. However, these methods provide direct estimations and are only useful for fully developed turbulent flows with large Reynolds values (Dyer, 1986). These methods do not entirely address the equipment and methodological inaccuracies, as they may have high uncertainties potentially reaching 50%. In contrast, numerical modelling of turbulent flows in open-channel bends may be a more suitable method as it provides a more streamlined evaluation of bed shear stress patterns (Abhari et al., 2010; Bai et al., 2014; Ghaneeizad et al., 2019). Studies using isotropic turbulence models including the standard and re-normalisation group k-ε models may provide relatively more accurate predictions. However, these models have limited predictive capabilities, particularly for secondary fluid motions, and the model may underestimate the flow separation zone, especially in sharp bends (Balen et al., 2009; Kang & Choi, 2010). Moreover, k–ε turbulence models were suggested to be unable to simulate the outer-bank cell compared with the Large Eddy Simulation (LES) method conducted by Booij (2003) in a 180°mild bend. Constantinescu et al. (2011) found that the bed shear stress distribution predicted by DES is significantly different than that predicted by RANS, while DES predictions of the mean flow are more accurate.

Although the Reynolds stress equation model (RSM) directly solves the Reynolds stress transport equations, it does not use the isotropic turbulence assumption. However, it provides advantages when simulating strong rotational flows. As large transverse water surface slopes are normally present in sharp open-channel bends. The adoption of rigid lid assumptions may result in flow field prediction errors, owing to incorrect pressure fields (Khosronejad et al., 2007). Hence, using the volume of fluid (VOF) method may provide the water surface variations of two-phase flow in numerical simulations (Han et al., 2011).

In this study, 180° open-channel bend with a curvature ratio of 3 was used to determine the underlying mechanisms related to the redistribution of the bed shear stress and roughness coefficient. Specifically, this study aimed to: (1) verify the efficacy and accuracy of the RSM and VOF methods in sharp bends simulation, (2) analyse the bed shear stress and roughness coefficient distribution throughout the bend, (3) identify the effect of circulation cells on the redistribution of bed shear stress, and (4) establish an expression for the resistance coefficient which reflects the spatial variation in bends.

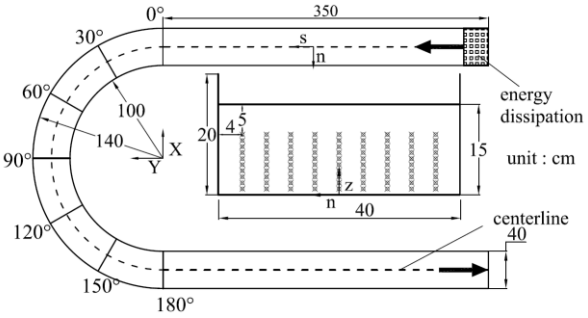

Fig. 1. Plan view of the laboratory flume and measuring grid.

2. INVESTIGATION METHODS

2.1 Experiments

Experiments were conducted in a 0.4 m wide plexiglass flume. The plane structure of the laboratory flume is shown in Fig. 1. The straight inflow and outflow reaches were 3.5m, which were joined to a 180° bend with the constant radius of curvature. The plane configuration was based on the middle reaches of Jinghe River located in the Loess Plateau in China. The scale of the test was 1:300, the width of the channel and the depth of the laboratory was determined according the actual landform. The curvature ratio ranged from 2.5-3.5, and we considered the constant curvature ratio (R/B=3), which was the typical representative of sharp channel bends. Table 1 lists the hydraulic conditions for the three experimental cases. The discharge (Q) ranged from 9–15 L/s, and H was constant. The discharge is determined according to the Froude similarity criterion. Reynolds number (Re) ranged from 23000–38000, and Froude number (Fr) ranged from 1.2–2,1, which indicates that the flow regimes were turbulent and subcritical.

During the experiment, the discharge in the circulating water system was unchanged. The discharge measurements were performed using a calibrated flow meter set on the supply water pump. The water surface level at the exit was controlled using a needle water level gauge and kept constant. Grilles were used for energy dissipation at the bend entrance. After the flow was stabilized, three-dimensional velocity vectors were measured using an Acoustic Doppler Velocimeter (ADV). ADV was fixed on a facility which can move up, down, left and right. The receivers of ADV were parallel to the direction of main flow. The velocity measuring accuracy is ± 0.5% and measuring error was less than 1mm/s The velocity sampling frequency was 200 Hz, withan

Table 1 Geometric and hydraulic conditions.

Cases	Q(L/s)	R(m)	B(m)	H(m)	U(m/s)	S(%)	B/H	R/B	$Re(10^4)$	Fr
1	9	1.2	0.4	0.15	0.15	0.08	2.7	3	2.3	0.12
2	12	1.2	0.4	0.15	0.2	0.08	2.7	3	3	0.16
3	15	1.2	0.4	0.15	0.25	0.08	2.7	3	3.8	0.21

acquisition time of 60 s. The water surface level was measured using the needle water level gauge. Measurements were performed at the 0°, 30°, 60°, 90°, 120°, 150°, and 180° sections. The grid used for the velocity-vector measurement is shown in Fig.1. The vertical spacing was set to 1 cm. The cylindrical coordinate system, which is shown in Fig.1, was used to analyse the experimental data. The s axis pointed downstream, and the n axis was perpendicular to s axis, pointing inwards, while the z axis was in a vertical position, pointing upwards.

2.2 Numerical Model

To obtain a more detailed flow characteristics, a 3D numerical simulation of the bend was performed by ANSYS FLUENT. The flow field was obtained by solving Reynolds-averaged Navier–Stokes (RANS) equations with the RSM turbulence closure approach. The water surface was captured by the VOF method. Wall functions were applied as the Reynolds value was low near walls.

Eqs. (1) and (2) are RANS equations (Dey 2014); Eq. (3) is the Reynolds stress-transport equation; Eqs. (4) and (5) are the turbulent kinetic energy equation and turbulence dissipation rate equation, respectively (ANSYS, 2011):

$$\frac{\partial(\rho)}{\partial t}+\frac{\partial(\rho u_i)}{\partial x_i}=0 \tag{1}$$

$$\frac{\partial(\rho u_i)}{\partial t}+\frac{\partial(\rho u_i u_j)}{\partial x_j}=-\frac{\partial p}{\partial x_j}+\frac{\partial}{\partial x_j}(\mu\frac{\partial u_i}{\partial x_j}-\rho\overline{u_i' u_j'}) \tag{2}$$

$$\frac{\partial(\rho\overline{u_i' u_j'})}{\partial t}+\frac{\partial(\rho u_k\overline{u_i' u_j'})}{\partial x_k}=\frac{\partial}{\partial x_k}(\frac{\mu_t}{\sigma_k}\frac{\partial\overline{u_i' u_j'}}{\partial x_k}+\mu\frac{\partial\overline{u_i' u_j'}}{\partial x_k}) -\frac{2}{3}\rho\varepsilon\delta_{ij}-P_{ij}+\Phi_{ij} \tag{3}$$

$$\frac{\partial(\rho k)}{\partial t}+\frac{\partial(\rho k u_i)}{\partial x_i}=\frac{\partial}{\partial x_j}((\frac{\mu_t}{\sigma_k}+\mu)\frac{\partial k}{\partial x_j})+\frac{1}{2}P_{ij}-\rho\varepsilon \tag{4}$$

$$\frac{\partial(\rho\varepsilon)}{\partial t}+\frac{\partial(\rho\varepsilon u_i)}{\partial x_i}=\frac{\partial}{\partial x_j}((\frac{\mu_t}{\sigma_\varepsilon}+\mu)\frac{\partial\varepsilon}{\partial x_j}) +\frac{1}{2}C_{1\varepsilon}P_{ij}-C_{2\varepsilon}\rho\frac{\varepsilon^2}{k} \tag{5}$$

where ρ is the density of water, u_i is the time-averaged velocity, u_i' is the fluctuating velocity, p is the fluid pressure, μ is the dynamic viscosity, k *and* ε represents the turbulent kinetic energy and turbulent dissipation rate, $\mu_t=C_\mu\rho k^2/\varepsilon$ is the eddy viscosity, δ_{ij} is the Kronecker delta, $P_{ij}=-\rho(\overline{u_i' u_k'}\partial u_j/\partial t+\overline{u_j' u_k'}\partial u_i/\partial t)$ is the production of

turbulent kinetic energy term, Φ_{ij} is the pressure strain term.

Structured meshes with hexahedral elements were used to fit the curved shape. A high-resolution grid consisting of 1074×83×47 points, approximately 4.2 million grid points in total, for the computational domain was applied. The grids used in the numerical model is shown in Fig. 2. Verification of the grid-independent solutions was conducted by increasing the grid number from 4.2 million to 6 million. The correlation coefficients of the two simulation results were greater than 99%, indicating that the former mesh was sufficient. The first near-wall grid was located in the logarithmic region that met the condition ($30<y^+=\Delta y u_\tau/\upsilon<100$, where u_τ represents the friction velocity, Δy represents the distance of the first grid to the wall, and υ represents the kinematic viscosity). The finite volume method (FVM) was applied to discretize control equations. Pressure-Implicit with Splitting of Operators (PISO) algorithm is applied and PRESTO! Format is adopted as pressure interpolation schemes. The standard wall function option of the ANSYS FLUENT was employed for the near-wall region modelling. The mass flow inlet and pressure outlet were also set. The bed and sidewall were set as solid walls that satisfied the no-slip condition. The interface between air and water phases was determined by the VOF method which calculates the fraction of water phase in the interface grid (Ferziger & Peric, 2002).

3. RESULTS AND DISCUSSIONS

3.1 Model Validation

The simulation results were validated using collected experimental laboratory data. The simulated and measured profiles of the streamwise, transverse, and vertical velocities in the 60° and 120° sections are shown in Fig. 3,

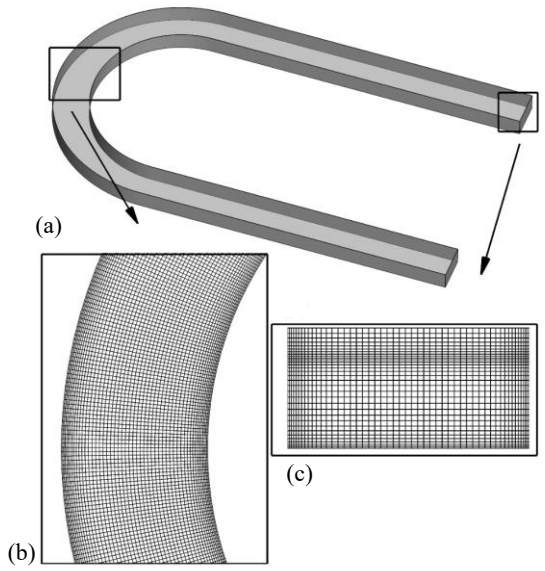

Fig. 2. View of grids used in the numerical model: (a) Numerical domain, (b) plane grids, (c) cross-sectional grids.

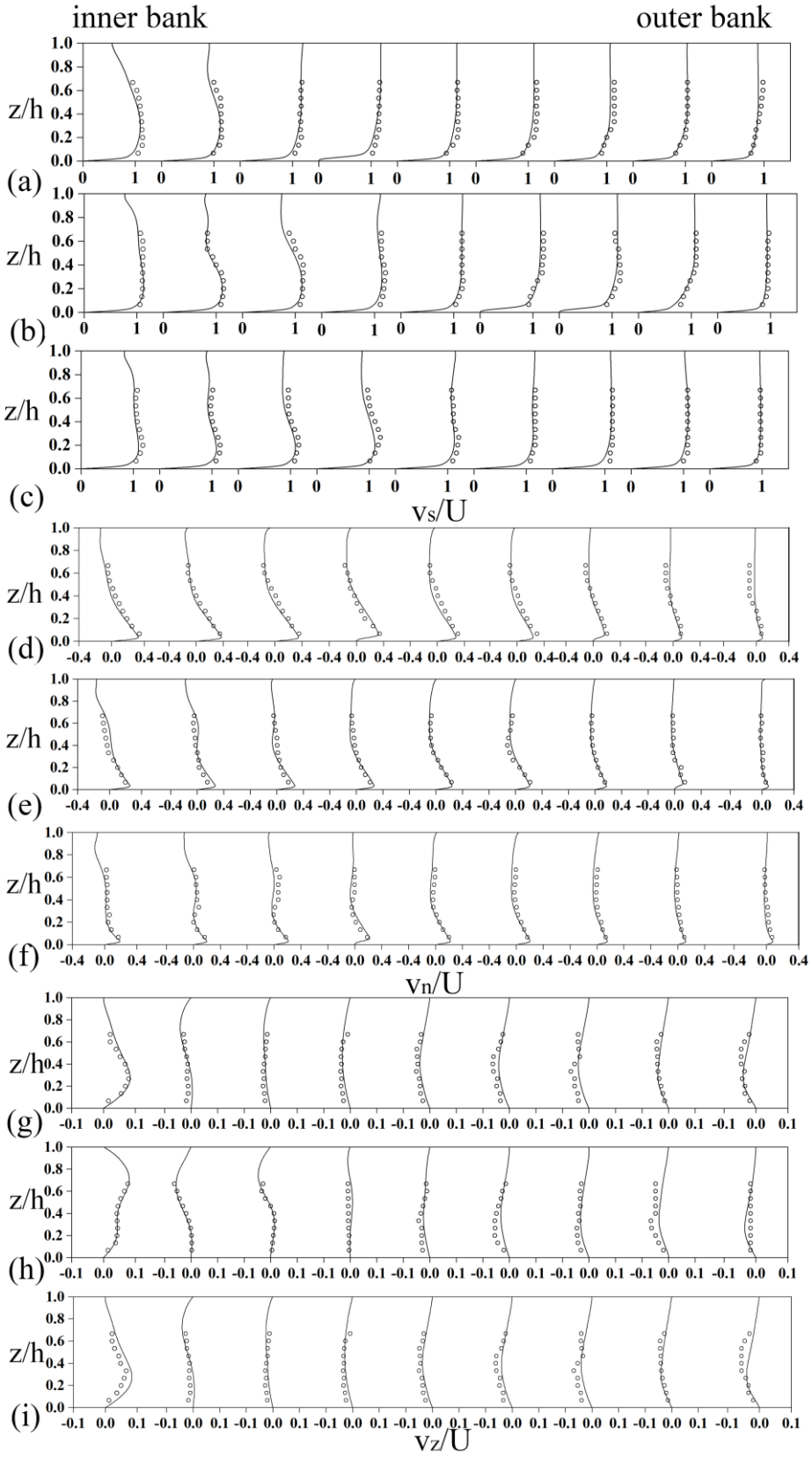

Fig. 3. Profiles of the simulated and measured velocities, normalized by the mean streamwise velocity(*U*) :(a) (d) (g) at the 60° section; (b) (e) (h) at the 90° section; (c) (f) (i) at the 120° section. Vs, Vn, and Vz are the streamwise velocities, transverse velocities, and vertical velocities, respectively. The lines represent the simulated value and the dots represent the measured value.

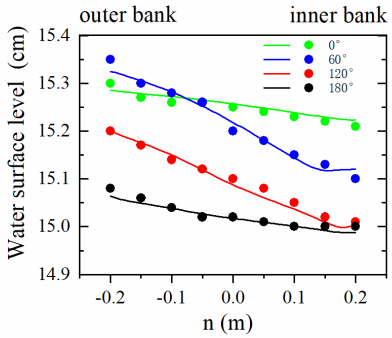

Fig. 4. Comparison of the simulated and measured water surface level. The lines represent the simulated value and the dots represent the measured value.

in which the measured velocities showed consistencies with the simulated velocities. The streamwise velocities did not follow a logarithmic distribution, owing to the influence of the secondary flows. In the 60° section, the maximum streamwise velocity appeared near the near-bed region. The transverse and vertical velocities reflected the circulation structures in the bend, and an apparent secondary flow exists with positive transverse velocities in the upper region, whereas negative transverse velocities were found in the near-bed region. The maximum transverse velocities were approximately 35% of the streamwise velocities, while the vertical velocities were approximately 5%. The distribution shape of the transverse velocities became more complex and large fluctuations appeared in the outer bank region, indicating that the out-bank cell had been generated. The vertical velocities exhibited an alternating pattern of upwelling and downwelling, which can be associated with the flow separation in the inner bank region.

The simulated and measured water surface levels at the 0°, 60°, 120° and 180° sections are shown in Fig. 4; the water surface developed a transverse tilting from the 0° section. The gradients of transverse water surface had an order of magnitude larger than that of the streamwise water surface. The simulated water surface level also fitted well with the measured value and corresponded to the law of bending.

The performance of the simulation was evaluated by normalised root mean square error (*NRMSE*) and Nash-Sutcliffe efficiency (*NSE*). The *NRMSE* and *NSE* are calculated by Eqs. (6) and (7) (Shcherbakov et al., 2013).

$$NRMSE = \sqrt{\frac{1}{m}\sum\left(y_i - \hat{y}_i\right)^2} \Big/ \left(y_{\max} - y_{\min}\right) \tag{6}$$

$$NSE = 1 - \frac{\sum\left(y_i - \hat{y}_i\right)^2}{\sum\left(y_i - \bar{y}_i\right)^2} \tag{7}$$

where m is the number of measured points; y_i , $\hat{y}_i$ represents the simulation and measured value, respectively; $\bar{y}_i$ represents the average measured value; and $y_{\max}$, $y_{\min}$ represents the maximum and minimum measured value, respectively.

Table 2 shows the *NRMSE* and *NSE* values for the different sections. For *NRMSE*, a lower value indicates higher efficiency. The value of *NSE* ranges from $-\infty$ to 1. $NSE = 1$ indicates a perfect performance, while $NSE = 0$ indicates that it is merely comparable to the mean value. The critical value of the velocity verification is normally 0.7. In this study, the *NRMSE* was observed to have a value of <0.1, while the *NSE* was >0.7 for all sections; this indicates that the RSM and VOF method can effectively simulates the flow characteristics.

3.2 . Bed Shear Stress Distribution

As shown in Fig. 5(a), the distribution of total bed shear stress (τ) indicated that it varied significantly throughout the bend. The zone of maximum bed shear stress appeared close to the inner bank from the 50° to 110° sections. The maximum value was also nearly twice the minimum value in the entrance zone. Here, the location of the maximum bed shear stress in the section gradually shifted outwards. As to the bend exit segment, it was close to the outer bank. This observed distribution pattern is due to the momentum transport caused by circulation structure developed along the bend. The velocity gradient near the bed increased, owing to the distortion of the streamwise velocity profiles. The velocity dip phenomenon was more apparent in the inner bank region in Fig. 3(a) and 3(b), which in turn formed a high value region. The distribution of bed shear stress shows a similar pattern with Kashyap et al. (2012) and Bai et al. (2014).

The total bed shear stress was divided into two components: the downstream bed shear stress (τ_{bs}) and

Table 2 Model performance validation

Sections	v_s		v_n		v_z		Water surface level	
	NRMSE	*NSE*	*NRMSE*	*NSE*	*NRMSE*	*NSE*	*NRMSE*	*NSE*
0°	0.020	0.838	0.048	0.850	0.044	0.750	0.090	0.932
30°	0.017	0.943	0.017	0.872	0.028	0.725	0.060	0.986
60°	0.027	0.918	0.016	0.881	0.022	0.779	0.100	0.934
90°	0.025	0.899	0.019	0.852	0.020	0.737	0.100	0.984
120°	0.037	0.860	0.031	0.720	0.032	0.762	0.080	0.995
150°	0.032	0.884	0.030	0.716	0.028	0.634	0.070	0.997
180°	0.026	0.761	0.021	0.722	0.060	0.750	0.050	0.952

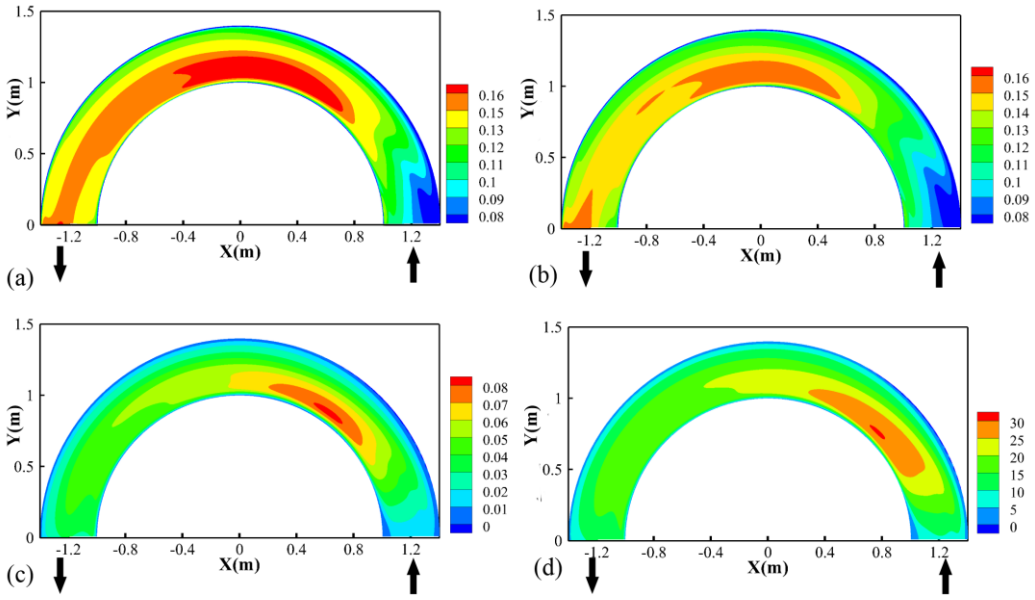

Fig. 5. Distribution of bed shear stress: (a) Bed shear stress (Pa)；(b) downstream component of bed shear stress (Pa)；(c) cross-stream component of bed shear stress (Pa), (d) angular deviation of the bed shear stress vector (°).

the transverse bed shear stress (τ_{bn}). Their distributions are shown in Fig. 5(b) and 5(c), respectively. The distribution of the former, which ranged from 0.07 to 0.15 Pa, was identical to that of the total bed shear stress, indicating that τ_{bs} is a major component that determines the bed shear stress pattern. Compared with τ_{bs} , τ_{bn} played only a secondary role. Although it only ranged from 0.01 to 0.08 Pa, its distribution had a direct influence on the bed shear stress direction as the zone of the maximum value of τ_{bn} appeared near the inner bank region from the 40° to 75° sections prior to τ_{bs} . The value of τ_{bn} in the inner bank region then became larger than that in the outer bank. Figure 5(d) illustrates the distribution of the angular deviation, $\theta_\tau = \arctan(\tau_{bn} / \tau_{bs})$. The average angle of deviation was 16°, and ranged from 5–30°. In the 45° section, the maximum value was achieved in addition to a distribution that was observed to be similar to that of τ_{bn} .

The outer bank cell (S2) which was shown in Fig.7 prevents τ from increasing outwards. It was in accord with the finding of Blanckaert and Graf (2004), which indicated that the existence of S2 induces a protective effect on banks. However, to further verify this, the transfer of momentum from free surface to bed region should be considered. The distribution of τ is essential for a qualitative understanding of scour patterns. Erosion occurs when the shear stress is higher than the critical value related to the sediment grain size directly. Therefore, the region of the maximum sediment grain size in transport would correspond to the zone of the maximum value of τ . In this study, region of low value of τ were observed to be pre-dominantly occupied by fine sediments. The magnitude of τ as well as direction have influences on the erosion and deposition in the channel bends as τ_{bn} tends to transport sediments inwards. Hence, to determine the transverse slope of river bed, a balance between the cross-stream component of τ and gravitational force acted on the bed materials should be first achieved (Blanckaert et al., 2008).

3.3 Contribution Rates of Terms in Momentum Equations

To investigate the underlying mechanisms of such inhomogeneous distribution, the depth-averaged momentum equations were derived from the Navier-Stokes equation under the assumption of a hydrostatic pressure distribution. The streamwise and transverse bed shear stress are expressed by Eq. (8) and Eq. (9) (Blanckaert & Graf, 2004; Termini, 2015):

$$\begin{aligned}\tau_{bs} = &-\rho\left[\frac{1}{1+n/R}\frac{\partial}{\partial s}(\langle v_s^{\,2}\rangle hn + \frac{\partial}{\partial n}(\langle v_s\rangle\langle v_n\rangle h) + \frac{2}{1+n/R}\frac{\langle v_s\rangle\langle v_n\rangle h}{R}\right]\Bigg\} TS1\\ &-\rho\left[\frac{\partial}{\partial n}\langle v_s^{*}v_n^{*}\rangle h + \frac{2}{1+n/R}\frac{\langle v_s^{*}v_n^{*}\rangle h}{R}\right]\Bigg\} TS2\\ &-\rho\left[\frac{1}{1+n/R}\frac{\partial}{\partial s}(\langle \overline{v_s'^{\,2}}\rangle h + \frac{\partial}{\partial n}(\langle \overline{v_s'v_n'}\rangle h) + \frac{2}{1+n/R}\frac{\langle \overline{v_s'v_n'}\rangle h}{R}\right]\Bigg\} TS3\\ &-\rho\left[\frac{1}{1+n/R}gh\frac{\partial n\, h + z_b n}{\partial s}\right]\Bigg\} TS4\end{aligned} \tag{8}$$

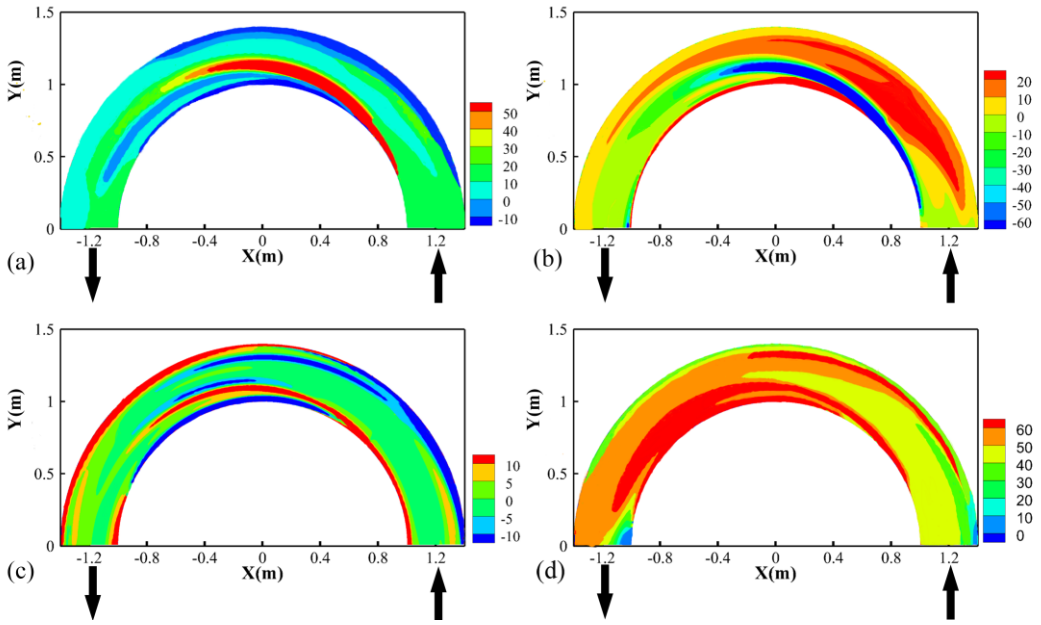

Fig. 6. Contribution rates of terms in depth-averaged momentum equations to the downstream component of bed shear stress:(a) *CRS1* (%), (b) *CRS2* (%), (c) *CRS3*(%), (d) *CRS4* (%).

$$
\begin{aligned}
\tau_{\mathrm{bn}} = -\rho & \left[\frac{1}{1+n/R}\frac{\partial}{\partial s}(\langle v_s\rangle\langle v_n\rangle h) + \frac{\partial}{\partial n}\left(\langle v_n\rangle^2 h\right) + \frac{1}{1+n/R}\frac{h(\langle v_n\rangle^2 - \langle v_s\rangle^2)}{R} \right] TN1 \\
-\rho & \left[\frac{1}{1+\mathrm{n}/R}\frac{\partial}{\partial s}\left(\langle v_s^* v_n^*\rangle h\right) + \frac{\partial}{\partial n}\left(\langle v_n^{*2}\rangle h\right) + \frac{1}{1+n/R}\frac{h(\langle v_n^{*2}\rangle - \langle v_s^{*2}\rangle)}{R} \right] TN2 \\
-\rho & \left[\frac{1}{1+n/R}\frac{\partial}{\partial s}\left(\langle \overline{v_s' v_n'}\rangle h\right) + \frac{\partial}{\partial n}\left(\langle \overline{v_n'^2}\rangle h\right) + \frac{1}{1+n/R}\frac{h(\langle \overline{v_n'^2}\rangle - \langle \overline{v_s'^2}\rangle)}{R} \right] TN3 \\
-\rho & \left[gh\frac{\partial \mathrm{n}\, h + z_b \mathrm{n}}{\partial n} \right] TN4
\end{aligned}
\tag{9}
$$

where g is the gravitational acceleration; h is the local water depth; and the brackets $\langle\ \rangle$ refer to the depth-averaged values. According to the approach used by Blanckaert and Graf (2004), the velocity components are decomposed by the equation: $v_i = \langle v_i\rangle + v_i^*$; this can result in separation of the cross-stream circulation from the translatory motion. v_n^* is the transverse component of the cross-stream circulation. $\langle v_n\rangle$ was defined as the cross-flow.

The right side of Eqs. (8) and (9) contain four terms, namely: *TS1* and *TN1*, *TS2* and *TN2*, *TS3* and *TN3*, *TS4* and *TN4*. *TS1* and *TN1* represent the inertial effects associated with the cross-flow and mainly include the corresponding advective momentum transport. Meanwhile, *TS2* and *TN2* represent the effect of cross-stream circulation; *TS3* and *TN3* represent the turbulent momentum transport; *TS4* and *TN4* represent the pressure gradient term in the tangential and radial directions, respectively. Based on detailed simulation results, these terms were evaluated and the contribution rate of each term was then calculated using Eq. (10) to analyse their corresponding roles in the determination of the bed shear stress:

$$
\begin{aligned}
CRSj &= TSj / \tau_{\mathrm{bs}}' \ 100\% \\
CRNj &= TNj / \tau_{\mathrm{bn}}' \ 100\%
\end{aligned}
\tag{10}
$$

where $j = 1, 2, 3, 4$; $CRSj$, and $CRNj$ are the contribution rates of each term in the tangential and radial directions, respectively.

As shown in Fig.6(a), the contribution rate of *TS1* to the downstream bed shear stress (*CRS1*) was approximately 20%. A maximum positive value of 50% was also obtained near the inner bank. As *CRS1* is related to the depth-averaged transverse velocity (<v_n>), flow separation would often occur near an inner bank. In this study, a flow separation region with lower velocities was present between the inner bank and high velocity cores (Blanckaert, 2015), accompanied by mass transport towards the outer bank owing to mass conservation. A large value of <v_n> near the inner bank accounted for the maximum positive value of *CRS1* in this region. The value of *CRS1* in the centre region was positive, indicating that the cross-flow increases the bed shear stress by momentum transport. Meanwhile, the opposite was presented in the outer bank region.

As shown in Fig.6 (b), the contribution rate of *S2* (*CRS2*) was of the same order as *CRS1*. The absolute value of *CRS2* was observed to be small in the bend entrance

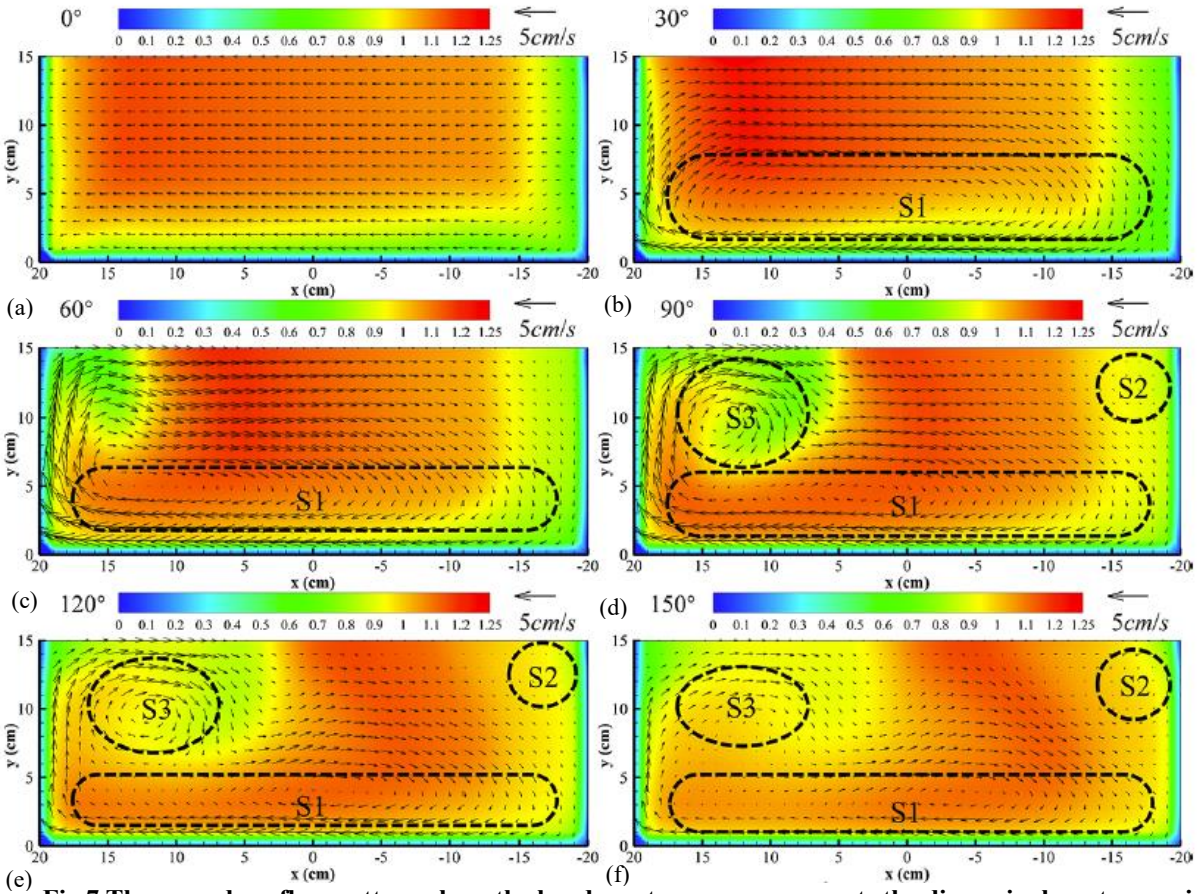

Fig.7 The secondary flow pattern along the bend, contour map represents the dimensionless streamwise velocities.

zone, ranging from -10% to 10%, where it also increased with the circulation development along the bend. The zone of maximum *CRS2* was located in the inner bank region from the 30°–120° sections, and the bed shear stress is strongly influenced by the cross-stream circulations in this region. The evolution of circulation cells is shown in Fig.7. In the 30° and 60° sections, one clockwise circulation cell (S1) was present which occupied almost the cross-section. In the 90° section, S2 was observed near the water surface in the outer bank region. Multiple circulation cells appeared from the 90°section. Here, the main circulation cell had an apparent split into two cells (S1 and S3). S3 was located in the inner bank region and the size of S3 increased from 90° to 150°sections. The high values of *CRS2* keeps some distance from the bank; this indicates that the counter-rotating cell prevented τ_{bs} from continually increasing toward the bank. The uneven distribution of *CRS2* also indicates that the cross-stream circulation had a significant impact on the redistribution of τ_{bs} .

Figure 6(c) and 6(d) illustrate the contribution rates of the turbulent momentum transport (*CRS3*) and pressure gradient term (*CRS4*). The average values of *CRS3* and *CRS4* were approximately 5% and 45%, respectively. The order of magnitude of the latter was observed to be larger than that of the former, indicating that the pressure gradient played a major role in determining the distribution of τ_{bs} . Here, the turbulent term can also be considered as negligible. The value of *CRS3* was predominantly negative in the outer bank and centre regions. Meanwhile, the value of *CRS4* was positive throughout the bend. *CRS4* in the outer bank and inner bank regions was also larger than that in the central region, indicating that the influence of the pressure gradient is more apparent in the bank region.

Figure 8 shows the contribution rates of *CRN1*, *CRN2*, *CRN3* and *CRN4* to the transverse bed shear stress. The average values obtained were approximately 30%, 7%, 3%, and 60%, respectively. The orders of magnitude of *CRN2* and *CRN3* were also smaller than those of *CRN1* and *CRN4*. It can be inferred that the pressure gradient term played a dominant role in the distribution of τ_{bn} as it behaved differently throughout the bend due to the varying transverse water surface gradient in different regions. As shown in Fig.4, the gradient in the inner bank is smaller than that in the outer bank.

Consistent with the findings obtained by Blanckaert & Graf (2004), both the cross-flow and cross-stream circulation played important roles in the downstream bed shear stress distribution, in addition to the pressure gradient term,

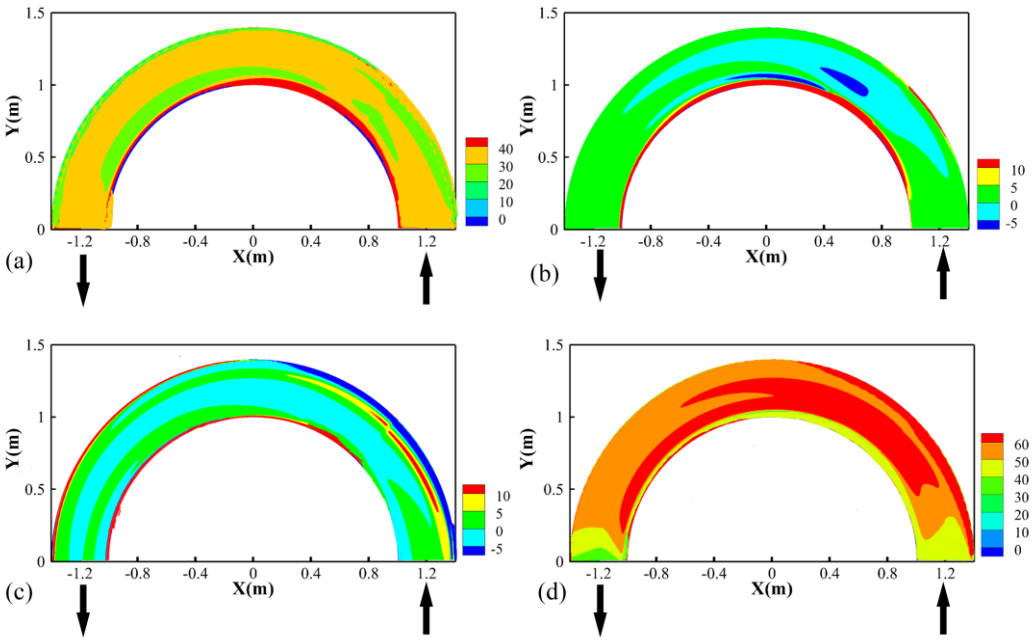

Fig. 8. Contribution rates of terms in depth-averaged momentum equations to the cross-stream component of bed shear stress: (a) *CRN1* (%), (b) *CRN2* (%), (c) *CRN3*(%), (d) *CRN4* (%).

which had an influence particularly in sharp open channel bends. However, Termini (2015) found the contribution of cross-flow is of an order of magnitude greater than that of cross-circulation. This difference may be attributed to the presence of a large transverse bed slope during the experiments, which enhanced the effect of inertia. Additionally, the bed topography also has a strong influence on distribution of τ , which in turn, is primarily determined by the bed shear stress.

3.4 Resistance Coefficient Distribution

Prediction of the bed shear stress is critically significant to address engineering issues in rivers. The bed shear stress is generally denoted by a Chézy-type resistance coefficient, which consequently relates τ to the flow velocities (Engel & Rhoads, 2016):

$$c = \sqrt{r\,g(\langle v_s \rangle^2 + \langle v_n \rangle^2)/\tau} \tag{11}$$

where c is the Chezy resistance coefficient.

The distribution of the resistance coefficients is shown in Fig. 9, which shows that the resistance coefficients had an uneven distribution throughout the bend, owing to the nonlinear interaction between the circulation cells and streamwise velocities. The Chezy resistance coefficient showed an overall downward trend along the bend. This coefficient also reflects energy losses; high energy loss corresponds to smaller values. In this study, the energy loss relatively increased along the bend with the development of cross-stream circulations. High Chezy resistance coefficients were initially observed at the bend inlet, owing to the absence of any circulation. According to Blanckaert (2009), increases in energy losses may be explained by three main mechanisms: the transverse shear stress arisen from the circulations, increased streamwise velocities gradients in the near-bed region, and enhanced

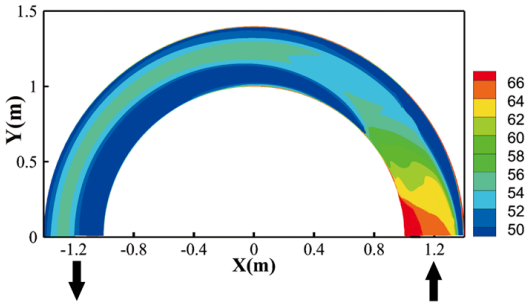

Fig. 9. Distribution of Chezy resistance coefficient.

turbulence production rate. The transverse distribution of the Chezy resistance coefficient behaved differently in the entrance zone and the rest of the bend due to the opposite transverse momentum transport directions. In the entrance zone, it increased inwards. The opposite was observed in the rest of the bend.

3.5 Expression for Chezy Resistance Coefficient

Based on the resistance coefficient distribution analysis in this study, the prediction of velocities, flow discharge, and shear stress was inaccurate when constant resistance coefficient was used in the depth-averaged flow model. Hence, a comprehensive expression for the Chezy resistance coefficient that considers the streamwise variation along the bend centreline and transverse variation needs to be established.

Considering the spatial variation in the bend, the Chezy resistance coefficient is often assumed as:

$$c = c_b\, f(r, R, \theta, \theta_0) \tag{12}$$

where r is the local radius; θ is the angle between the

local section and entry section; θ_0 is the centre angle of the bend; and function f denotes the bend-induced spatial distribution coefficient. $c_b = (\sqrt{g}/\kappa)\ \ln(11h/k_s)$ represents the Chezy resistance coefficient in straight channels (Da Silva, 1999). It is mainly affected by the relative roughness (h/k_s) for fully developed turbulent flows (Yen, 2002). In this equation, h represents the average water depth, κ represents the Von Karman constant, and k_s represents the effective bed roughness. The effective bed roughness used in our study is 0.03mm, which is assumed to be proportional to a representative sediment size ($k_s = 3.5D_{84}$), where D_{84} refers to the diameter of the grain composed of 84% are fine particles.

The (r,θ) coordinate system can be transformed from the (s,n) coordinate system. The two dimensionless parameters (r/R, θ/θ_0) were obtained to express the spatial variation in the bend. The function $f(r/R,\theta/\theta_0)$ can then be divided into two components:

$$f(r/R,\theta/\theta_0)=g(\theta/\theta_0)\cdot(r/R)^{h(\theta/\theta_0)} \tag{13}$$

where $g(\theta/\theta_0)$ represents the streamwise variation along the centreline, and $(r/R)^{h(\theta/\theta_0)}$ represents the transverse variation in consideration with the comprehensive effect of r and q.

The functions of $g(\theta/\theta_0)$ and $h(\theta/\theta_0)$ were assumed as:

$$g(\theta/\theta_0)=\mathrm{k}_1(\theta/\theta_0)+\mathrm{k}_2 \tag{14}$$

$$h(\theta/\theta_0)=\cos(\mathrm{k}_3(\theta/\theta_0)+\mathrm{k}_4) \tag{15}$$

where k_1, k_2, k_3, and k_4 are constant parameters estimated according to the 0°, 60°, 90°, 120°, and 180° sections in Case 2. The optimal values were $\mathrm{k}_1 = -0.2$, $\mathrm{k}_2 = 0.8$, $\mathrm{k}_3 = -4\pi/3$, and $\mathrm{k}_4 = \pi$.

The Chezy resistance coefficient in bends is expressed as

$$c = (-0.2(\theta/\theta_0)+0.8)(r/R)^{-\cos(4/3\pi\,(\theta/\theta_0))}\sqrt{g}/\kappa\ln(11h/k_s) \tag{16}$$

In addition to the calculated values based on the simulation results of the three cases, a comparison of the Chezy resistance coefficient roughness predicted using Eq. (16) is also shown in Fig. 10. The predicted value was found to be consistent with the calculated value, suggesting that Eq. (16) can sufficiently estimate the resistance coefficient and accurately reflect a heterogeneous distribution. Consequently, this expression can be applied to improve the depth-averaged 2D numerical simulations related to curved rivers as it considers the streamwise variation along the centreline and transverse variation.

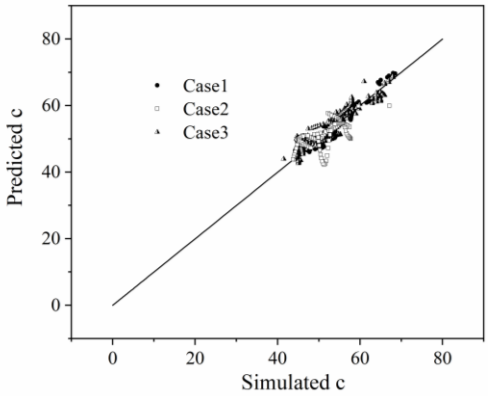

Fig. 10. Comparison of Chezy resistance coefficient predicted with simulation results.

4. CONCLUSION

In this study, the bed shear stress and roughness coefficient distributions in a sharp open-channel bend were investigated. A 3D numerical simulation was performed and verified using experimental data. The main conclusions are summarised as follows.

The RSM combined with the VOF method can effectively and precisely simulate the flow characteristics in sharp open channel bends. The simulated results indicated that the bed shear stress varied significantly throughout the bend. The zone of maximum bed shear stress was found near the inner bank from the 50° to 110° sections, which then gradually shifted outwards as cross-stream circulations developed. τ_{bs} is a major component that determines the bed shear stress pattern and τ_{bn} influences the direction.

The underlying mechanisms of the redistribution of τ_{bs} and τ_{bn} were also explored by quantitatively analysing the contribution rates of expression terms in the momentum equations to the bed shear stress. *CRS2* was of the same order as *CRS1*. The maximum *CRS2* was located near the inner bank from the 30° to 120°cross-sections. The advective momentum transport by cross-stream circulation also contributed to the redistribution of τ_{bs}. Meanwhile, the distribution of *CRS2* was mainly related to the circulation structure developed along the bend. The pressure gradient term also played a dominant role in determining τ_{bn}, owing to the large transverse water surface gradient in sharp open-channel bends.

The Chezy resistance coefficient demonstrated an overall decreasing trend along the bend, indicating increasing energy losses as secondary flows developed. It also increased inwards in the entrance zone, while the opposite was observed for the rest of the bend, and this may be attributed to the transverse momentum transport. Hence, this study successfully established an effective expression considering streamwise variation along the centreline and transverse variation to predict the uneven distribution of the Chezy resistance coefficient in sharp

open-channel bends.

This research provides insights into the underlying mechanisms of the bed shear stress distribution in bends with a flat-bed topography. The expression for the Chezy resistance coefficient developed in this study may improve depth-averaged 2D numerical simulations related to curved rivers. However, a series of movable bed experiments is necessary to further determine the interaction between the bed topography and bed shear stress.

ACKNOWLEDGMENTS

This study was funded by the National Natural Science Foundation of China (grant no. 11972265).

CONFLICT OF INTEREST

All authors have no conflicts to disclose.

AUTHORS CONTRIBUTION

All authors contributed to the study conception and design. Material preparation, data collection and analysis were performed by Peng Hu. The first draft of the manuscript was written by Peng Hu. Minghui Yu validated the results and reviewed the original draft of this paper.

REFERENCES

Abhari, M. N., Ghodsian, M., Vaghefi, M., & Panahpur, N. (2010). Experimental and numerical simulation of flow in a 90° bend. *Flow Measurement and Instrumentation,* 21(3), 292-298. https://www.doi.org/10.1016/j.flowmeasinst.2010.03.002

Abduo, S. S., Elmoustafa, A. M., & Salam, M. S. A. (2021). Study of counteracting the secondary flow in open channel bends. *Ain Shams Engineering Journal,* 12(3), 2425-2433 https://www.doi.org/10.1016/j.asej.2021.01.011

ANSYS (2011). ANSYS fluent 14.0 user's guide. ANSYS Inc, Canonsburg, PA.

Booij, R. (2003). Measurements and large eddy simulations of the flows in some curved flumes. *Journal of Turbulence,* 4(1), 8 https://www.doi.org/10.1088/1468-5248/4/1/008

Balen, W. V., Uijttewaal, W. S. J., & Blanckaert, K. (2009). Large-eddy simulation of a mildly curved open-channel flow. *Journal of Fluid Mechanics,* 630, 413-413. https://www.doi.org/10.1017/S0022112009007277

Bai, Y. C., Song, X. L., & Gao, S. X. (2014). Efficient investigation on fully developed flow in a mildly curved 180° open-channel. *Journal of Hydroinformatics,* 16(6), 1250-1264. https://www.doi.org/10.2166/hydro.2014.108

Blanckaert, K., & Graf, W. H. (2004). Momentum transport in sharp open-channel bends. *Journal of Hydraulic Engineering,* 130(3), 186-198. https://www.doi.org/10.1061/(asce)0733-9429(2004)130:3(186)

Blanckaert, K., & De Vriend, H. J. (2005). Turbulence characteristics in sharp open-channel bends. *Physics of Fluids,* 17(5), 055102. https://www.doi.org/10.1063/1.1886726

Blanckaert, K., Buschman, F. A., Schielen, R., & Wijbenga, J. H. (2008). Redistribution of velocity and bed-shear stress in straight and curved open channels by means of a bubble screen: Laboratory experiments. *Journal of Hydraulic Engineering,* 134(2), 184-195. https://www.doi.org/10.1061/(asce)0733-9429(2008)134:2(184)

Blanckaert, K. (2009). Saturation of curvature-induced secondary flow, energy losses, and turbulence in sharp open-channel bends: laboratory experiments, analysis, and modeling. *Journal of Geophysical Research: Earth Surface,* 114, F03015. https://www.doi.org/10.1029/2008JF001137

Blanckaert, K. (2011). Hydrodynamic processes in sharp meander bends and their morphological implications, *Journal of Geophysical Research: Earth Surface,* 116, F01003. https://www.doi.org/10.1029/2010JF001806

Blanckaert, K. (2015). Flow separation at convex banks in open channels. *Journal of Fluid Mechanics,* 779, 432-467. https://www.doi.org/10.1017/jfm.2015.397

Crosato, A. (2008). *Analysis and Modelling of River Meandering*. Ph. D. thesis. Delft University of Technology, Delft, Netherlands.

Constantinescu, G., Koken, M., & Zeng, J. (2011). The structure of turbulent flow in an open channel bend of strong curvature with deformed bed: Insight provided by detached eddy simulation. *Water Resources Research, 47*, W05515. https://www.doi.org/10.1029/2010WR010114

Dietrich, W. E., Smith, J. D., & Dunne, T. (1979). Flow and sediment transport in a sand bedded meander. *Journal of Geology,* 87, 305–315. https://www.doi.org/10.1086/628419

da Silva, A. M. A. F. (1999). Friction factor of meandering flows. *Journal of Hydraulic Engineering,* 125(7), 779-783. https://www.doi.org/10.1061/(asce)0733-9429(1999)125:7(779)

Dey, S., & Das, R. (2012). Gravel-bed hydrodynamics: a double-averaging approach. *Journal of Hydraulic Engineering,* 138(8), 707–725. https://www.doi.org/10.1061/(asce)hy.1943-7900.0000554

Dey, S. (2014). *Fluvial Hydrodynamics: Hydrodynamic and Sediment Transport Phenomena.* Springer, Berlin.

Dyer, K. R. (1986). *Coastal and Estuarine Sediment Dynamics*. Wiley, Chichester.

Engel, F. L., & Rhoads, B. L. (2016). Three-dimensional flow structure and patterns of bed shear stress in an evolving compound meander bend. *Earth Surface Processes & Landforms,* 41(9), 1211-1226. https://www.doi.org/10.1002/esp.3895

Farhadi, A., C. Sindelar, M. Tritthart, M. Glas, K. Blanckaert and H. Habersack (2018). An investigation on the outer bank cell of secondary flow in channel bends. *Journal of Hydro-Environment Research* 18, 1-11. https://www.doi.org/10.1016/j.jher.2017.10.004

Ferziger, J. H., & Peric, M. (2002). *Computational Methods for Fluid Dynamics*. Springer, Heidelberg.

Galperin, B., Kantha, L. H., Hassid, S., & Rosati, A. (1988). A quasi-equilibrium turbulent energy-model for geophysical flows. *Journal of the Atmospheric Sciences,* 45(1), 55-62. https://www.doi.org/10.1175/1520-0469(1988)045<0055:AQETEM>2.0.CO;2

Ghaneeizad, S. M., Bahrami Jovein, E., Abrishami, J., & Atkinson, J. F. (2019). Redistribution of flow velocity in sharp bends using unsubmerged vanes. *International Journal of River Basin Management,* 17(1), 49-61. https://www.doi.org/10.1080/15715124.2017.1411928

Han, S. S., Biron, P. M., & Ramamurthy, A. S. (2011). Three-dimensional modelling of flow in sharp open-channel bends with vanes. *Journal of Hydraulic Research*, 49(1), 64-72. https://www.doi.org/10.1080/00221686.2010.534275

Hooke, R. B. (1975). Distribution of Sediment Transport and Shear Stress in a Meander Bend. *The Journal of Geology*, 88(5), 543-565. https://www.doi.org/10.1086/628140

Hu, C., Yu, M., Wei, H., & Liu, C. (2019). The mechanisms of energy transformation in sharp open-channel bends: Analysis based on experiments in a laboratory flume. *Journal of Hydrology,* 571, 723-739. https://www.doi.org/10.1016/j.jhydrol.2019.01.074

Ippen, A. T., & Drinker, P. A. (1962). Boundary shear stresses in curved trapezoidal channels. *Journal of the Hydraulics Division,* 88(5), 143-179. https://www.doi.org/10.1061/jyceaj.0000772

Kim, S. C., Friedrichs, C. T., Maa, P. Y., & Wright L. D. (2000). Estimating bottom stress in tidal boundary layer from acoustic doppler velocimeter data. *Journal of Hydraulic Engineering,* 126(6), 399-406.

Krishnappan, B. G., & Engel, P. (2004). Distribution of bed shear stress in rotating circular flume. *Journal of Hydraulic Engineering,* 130(4), 324-331 https://www.doi.org/10.1061/(asce)0733-9429(2004)130:4(324)

Khosronejad, A., Rennie, C. D., Neyshabouri, S. A. A. S. & Townsend, R. D. (2007). 3D numerical modeling of flow and sediment transport in laboratory channel bends. *Journal of Hydraulic Engineering,* 133(10), 1123–1134. https://www.doi.org/10.1061/(asce)0733-9429(2007)133:10(1123)

Kang, H., & Choi, S. U. (2010). Reynolds stress modelling of rectangular open-channel flow. *International Journal for Numerical Methods in Fluids,* 51(11), 1319-1334. https://www.doi.org/10.1002/fld.1157

Kashyap, S., Constantinescu, G., Rennie, C. D., Post, G., & Townsend, R. (2012). Influence of channel aspect ratio and curvature on flow, secondary circulation, and bed shear stress in a rectangular channel bend. *Journal of Hydraulic Engineering,* 138(12), 1045-1059. https://www.doi.org/10.1061/(asce)hy.1943-7900.0000643

Nanson, R. A. (2010). Flow fields in tightly curving meander bends of low width-depth ratio. *Earth Surface Processes and Landforms,* 35, 119–135. https://www.doi.org/10.1002/esp.1878

Ottevanger, W., Blanckaert, K., & Uijttewaal, W. S. (2012). Processes governing the flow redistribution in sharp river bends. *Geomorphology,* 163, 45-55. https://www.doi.org/10.1016/j.geomorph.2011.04.049

Shcherbakov, M. V., Brebels, A., Shcherbakova, N. L., Tyukov, A. P., Janovsky, T. A., and Kamaev, V. A. E. (2013). A survey of forecast error measures. *World Applied Sciences Journal,* 24, 171-176. https://www.doi.org/10.5829/idosi.wasj.2013.24.itmies.80032

Thompson, C. E., Amos, C. L., Jones, T. E. R., & Chaplin, J. (2003). The manifestation of fluid-transmitted bed shear stress in a smooth annular flume-a comparison of methods. *Journal of Coastal Research*, 1094-1103. https://eprints.soton.ac.uk/1340/

Termini, D. (2015). Momentum transport and bed shear stress distribution in a meandering bend: Experimental analysis in a laboratory flume. *Advances in Water Resources,* 81,128-141. https://www.doi.org/10.1016/j.advwatres.2015.01.005

Van Balen, W., Uijttewaal, W. S., & Blanckaert, K. (2009). Large-eddy simulation of a mildly curved open-channel flow. *Journal of Fluid Mechanics,* 630, 413-442. https://www.doi.org/10.1017/S0022112009007277

Vaghefi, M., Akbari, M., & Fiouz, A. R. (2014). Experimental investigation on bed shear stress distribution in a 180 degree sharp bend by using depth-averaged method. *International Journal of*

Scientific Engineering and Technology, 3(7), 962-966. http://www.ijset.com/publication/v3/217.pdf

Vaghefi, M., Akbari, M., & Fiouz, A. R. (2016). An experimental study of mean and turbulent flow in a 180 degree sharp open channel bend: Secondary flow and bed shear stress. *Journal of Civil Engineering,* 20(4), 1582-1593. https://www.doi.org/10.1007/s12205-015-1560-0

Yen, B. C. (2002). Open channel flow resistance. *Journal of Hydraulic Engineering,* 128(1), 20-39. https://www.doi.org/10.1061/(asce)0733-9429(2002)128:1(20)

Yen, C. L., & Ho, S. Y. (1990). Bed evolution in channel bends. *Journal of Hydraulic Engineering,* 116(4), 544-562. https://www.doi.org/10.1061/(asce)0733-9429(1990)116:4(544)